An update to this article is included at the end

Journal of Photochemistry & Photobiology A: Chemistry 401 (2020) 112748

Contents lists available at ScienceDirect

Journal of Photochemistry & Photobiology A: Chemistry

journal homepage: www.elsevier.com/locate/jphotochem

Photocatalytic performance of titanium dioxide and zinc oxide binary system on degradation of humic matter

Nazli Turkten[a,*], Miray Bekbolet[b]

[a] Department of Chemistry, Faculty of Arts and Sciences, Kirsehir Ahi Evran University, Kirsehir 40100, Turkey
[b] Institute of Environmental Sciences, Bogazici University, Bebek, Istanbul 34342, Turkey

ARTICLE INFO

Keywords:
Binary oxide
ZnO/TiO_2
Humic acid
Photocatalysis

ABSTRACT

Application of photocatalysis using TiO_2 or ZnO for the removal of natural organic matter (NOM) dates back more than two decades. Aiming to overcome the drawbacks of sole photocatalysts, use of multiphasic systems has received recent interest. ZnO/TiO_2 binary oxide specimens were synthesized by a simple solid state dispersion method in different weight ratios of 1:1; 1:3; and 3:1 (ZT11, ZT13 and ZT31 respectively) and characterized by XRD, SEM, XPS, Raman, UV-DRS, PL and BET techniques. As a surrogate of NOM, humic acid (HA) was subjected to solar photocatalysis and degradation was followed by UV–vis and fluorescence spectroscopic tools along with dissolved organic carbon (DOC) contents. Photocatalytic degradation of HA was approximated to first order kinetic model. Referring to UV–vis parameters, ZT11 binary oxide expressed slightly higher photocatalytic performance with regard to TiO_2, ZnO, ZT13 and ZT31 contrary to the mineralization extents as TiO_2 > ZT13 > ZT31 > ZT11 > ZnO. Excitation-emission matrix fluorescence (EEM) contour plots of the organic matrix displayed almost complete removal of humic-like and fulvic-like fluorophores upon use of sole TiO_2 and ZnO. Regional distribution of the fluorophores were still evident with emergence of the new fluorophoric regions upon use of binary oxides. ZnO/TiO_2 could be considered as an efficient photocatalyst for the degradation of humic acids under solar irradiation.

1. Introduction

Semiconductor photocatalysis has been extensively investigated for almost 50 years. Significant interest was directed to the oxidation of pollutants and destruction of microorganisms both in aqueous medium as well as in air. The primary step of photocatalysis is recognized as the absorption of light with energy greater than the band gap energy (E_{bg}, eV) of the photocatalyst [1]. Through formation of e^-/h^+ pair and subsequent reactions with O_2 and H_2O, reactive oxygen species (ROS) are formed leading to various redox reactions. A simplified mechanism could be expressed as follows:

Photocatalyst (TiO_2/ZnO) + $h\nu \rightarrow h_{VB}^+ + e_{CB}^-$

$h_{VB}^+ + H_2O \rightarrow OH^{\cdot} + H^+$

$e_{CB}^- + O_2 \rightarrow O_2^{\cdot}$-

$O_2^{\cdot -} + H^+ \rightarrow HO_2^{\cdot}$

$2HO_2^{\cdot} \rightarrow H_2O_2 + O_2$

$H_2O_2 + e_{CB}^- \rightarrow OH^{\cdot} + OH^-$

ROS ($OH^{\cdot}$/ $O_2^{\cdot -}$/ $HO_2^{\cdot}$..) + organic matter (NOM/HAs..) → → intermediate degradation products (lower molecular size fractions/oxidized) →→..... → $CO_2 + H_2O$

Following photo-excitation and in case of lack of quick scavenging, h_{VB}^+ and e_{CB}^- recombination may occur within picoseconds via dissipation of enerygy (heat) leading to a decrease in quantum efficieny. Recombination may be reduced by various strategies as modifications and/or by heterogeneous coupling of the photocatalysts.

TiO_2 is regarded as a quintessential photocatalyst due to its specific properties such as being biocompatable, abundantly available, highly stable, low cost, low operation temperature and water insolubility [2–4]. The photocatalytic activity of TiO_2 is dependent on its surface and structural properties *i.e.* crystal composition, surface area, particle size distribution, porosity, band gap and surface hydroxyl density [5].

Band gap energies of the two crystal forms of TiO_2 were reported as 3.23 eV and 3.10 eV for anatase and rutile respectively. Thus, the major disadvantage of TiO_2 is the utilization of UV light excluding the advantage of harvesting visible light. In this respect, changing the

* Corresponding author.
E-mail address: nazli.turkten@ahievran.edu.trand (N. Turkten).

https://doi.org/10.1016/j.jphotochem.2020.112748
Received 2 October 2019; Received in revised form 24 February 2020; Accepted 3 July 2020
Available online 04 July 2020
1010-6030/ © 2020 Published by Elsevier B.V.

electrical properties and inducing batho-chromic shift of the band gap of TiO_2 were widely applied by metal/non-metal doping, surface modifications and sensitization.

ZnO is considered as the second widely used photocatalyst having a broad direct band gap energy ($E_{bg} = \sim 3.3$ eV). ZnO also exhibits excellent photocatalytic activity, antifouling and antibacterial properties [6]. Since ZnO has comparable band gap energy to TiO_2, similar primary steps in mechanism of photocatalytic activity could be anticipated [7]. ZnO can also express better photocatalytic performance since the electron mobility of ZnO ($200-300\ cm^2/Vs$) is higher than that of TiO_2 ($0.1–4.0\ cm^2/Vs$) contributing to high quantum efficiency. The position of the VB_{ZnO} is lower than that of VB_{TiO2} therefore the oxidation potential of hydroxyl radical generated by ZnO is higher than that of hydroxyl radical produced by TiO_2 leading to better photocatalytic performance [8].

Coupling of two semiconductor metal oxides such as M_xO_y/Me_zO_t (where M and Me represent the metal type and x, y, z, and t are the oxidation states in these metal oxides) has also gained attention to improve photocatalytic activity through higher light absorption capacity, and better suppression of photoinduced electron hole pair recombination thereby maintaining increased charge separation [9–11]. TiO_2 and ZnO as benchmarks of UV photocatalysis could be coupled for efficient utilization solar light as well as for modification of surface properties such as surface area, mesoporosity, crystallinity and morphology. TiO_2/ZnO composites were mostly prepared by sol-gel methodology by using various Zn precursors as zinc carbonate, zinc nitrate, zinc acetate and zinc citrate [12–16]. On the other hand, substrates used for activity testing were mainly dyes *i.e.*, methyl orange [14,17–24] methylene blue [25–27], brilliant golden yellow, C.I. Basic Blue 41, Procion Red MX-5B, C.I. Basic Red 1, C.I. Basic Violet 10, C.I. Basic Blue 3, C.I. Basic Blue 9, C.I. Basic Red 1 [12,13,15,13–16,28,29] and rhodamine B [30]. Organic substrates were 4-chlorophenol [31,32] and 4-nitrophenol [15,17]. Elucidation of photocatalytic performance was also extended to antibacterial activity testing using Gram-negative bacteria as *E. coli* and *P. aeruginosa*; and Gram-positive bacteria as *S. aureus*, methicillin-resistant *S. aureus*, *B. cereus* and anaerobic *C. perfringens* [16,33]. Photocatalytic inactivation studies were carried out by using *E. coli* [34]. However, research studies were not extended to the use of these photocatalysts for the elimination of natural organic matter as the major undesirable component of natural waters due to adverse effects on drinking water quality.

From public health point of view, the presence of NOM in water poses significant problems especially in terms of disinfection by-product formation potentials [35]. Therefore, the removal of NOM holds prime importance for obtaining safe drinking water. Application of photocatalysis for successful degradation of NOM has been the major concern of Bekbolet and co-workers since two decades [36–41]. On this purpose, further interest was directed to the application of binary oxides prepared by a simple solid state dispersion method for the degradation of humic acids (HA) as the model compound of NOM.

2. Methodology

2.1. Photocatalyst preparation and characterization

ZnO/TiO_2 binary oxides were synthesized by solid state dispersion method using ZnO (Aldrich) and TiO_2 (P-25, Evonik). Three different binary oxides with weight ratios of ZnO/TiO_2 as 1:1, 1:3 and 3:1 were prepared and represented as ZT11, ZT13 and ZT31 respectively. All binary oxides were calcined at 773 K for 1 h, grinded and stored in dark.

X-ray diffraction (XRD) patterns were recorded on a Rigaku-D/MAX-Ultima diffractometer using Cu Kα radiation ($\lambda = 1.54$ Å) operating at 40 kV and 40 mA and scanning rate $2^\circ\ min^{-1}$ at 2θ in the range $3-70^\circ$.

Scanning electron microscopy (SEM) was employed on an ESEM-FEG/EDAX Philips XL-30 instrument operating at 20 kV using catalyst powders supported on carbon tape.

X-ray photoelectron spectroscopy (XPS) was performed on a Thermo Scientific K-Alpha X-ray Photoelectron Spectrometer equipped with hemispherical electron analyzer and Al-Kα micro-focused monochromator.

Raman spectra were acquired by a Thermo Scientific DXR Raman Microscope using Ar^+ laser excitation at $\lambda = 532$ nm, laser power 10 mW and spectral resolution 2 cm^{-1}.

UV–vis diffuse reflectance spectra (UV–vis DRS) were obtained using a UV-2450, Shimadzu UV–vis spectrophotometer equipped with an integrated sphere reflectance accessory.

Photoluminescence (PL) measurements were performed using Perkin Elmer LS 55 Luminescence Spectrometer. Samples (0.25 mg/mL) were dispersed in 50 ml ethanol. Excitation wavelength was adjusted to 325 nm and emission intensities were recorded in the wavelength region of 350 nm–600 nm.

Specific surface area was determined using multi-point BET analysis. Pore size and pore volume were measured by BJH method. Nitrogen adsorption/desorption isotherm was obtained at liquid nitrogen temperature 77 K by using a Quantochrome Nova 2200e automated gas adsorption system.

2.2. Humic acid preparation and characterization

Commercial HA (Na salt) was purchased from Aldrich. HA (50 mg/L) was dissolved in distilled water and pre-filtered through 0.45 μm membrane filter (Millipore) to exclude any undissolved suspended humic matter. 100 kDa molecular size fraction of HA was prepared by ultrafiltration using 100 kDa molecular size cut-off membrane filter (Amicon 8050 ultrafiltration stirred cell unit) [42].

Spectroscopic measurements were performed by using Perkin Elmer Lambda 35 UV–vis double beam spectrophotometer and Perkin Elmer LS 55 Luminescence Spectrometer [39]. Specified UV–vis spectroscopic parameters were $Color_{436}$, UV_{365}, UV_{280} and UV_{254}. Fluorescence spectroscopic parameters were Fluorescence index (FI) and Excitation Emission Matrix (EEM) fluorescence contour plots. Specific carbon based UV–vis parameters as $CbColor_{436}$, $CbUV_{365}$, $CbUV_{280}$, and $CbUV_{254}$ as well as specific fluorescence index (SFI) were expressed by normalizing the respective spectroscopic parameters to DOC contents. DOC (mg/L) was determined as non-purgeable organic carbon by using Total Organic Carbon Analyzer Shimadzu TOC VWP. The reproducibility of the results was ≤ 5 %.

2.3. Solar photocatalytic treatment

Solar photocatalysis was performed by ATLAS Suntest CPS + simulator equipped with an air cooled Xenon lamp ($250\ W/m^2$ and wavelength range of $300-800$ nm) as the light source (Ref. 56052371, Atlas CPS + Solar Simulator). Photocatalyst specimens were removed from the reaction medium by immediate filtration through 0.45 μm membrane filter. Clear samples were subjected to UV–vis and fluorescence spectroscopic analyses as well as DOC determinations.

Particle size distribution was measured by time-resolved Dynamic Light Scattering (DLS) on the Brookhaven 90 Plus/BI-MAS Instrument.

3. Results and discussion

3.1. Characterization of the photocatalyst specimens

All photocatalyst specimens were characterized with reference to the described techniques [43].

X-ray diffractograms of ZnO, TiO_2 and ZnO/TiO_2 binary oxides were examined and presented in Fig. 1. In sole TiO_2 diffractogram, characteristic peaks of (1 0 1) plane of anatase and (1 1 0) plane of rutile were evidenced at 2θ values of 25.36° and 27.52° respectively. Eight distinctive peaks at 2θ values of 37.08°, 37.89°, 38.69°, 48.08°, 53.98°,

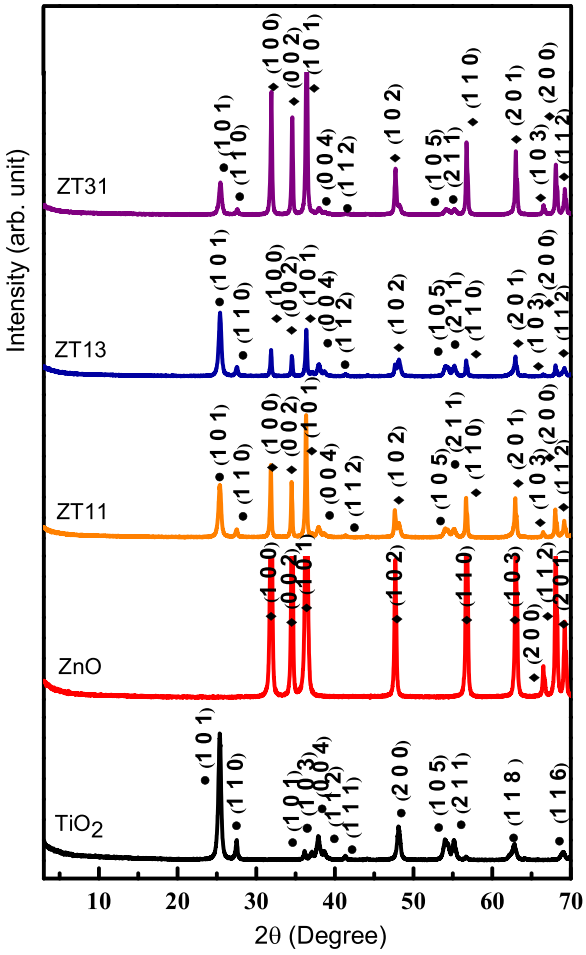

Fig. 1. XRD diffractograms TiO_2, ZnO and ZnO/TiO_2 binary oxides ZT11, ZT13 and ZT31. (• TiO_2, ♦ ZnO).

55.12°, 62.82°, 69.09° corresponding to (1 0 3) (0 0 4), (1 1 2), (2 0 0), (1 0 5), (2 1 1), (1 1 8) and (1 1 6) planes of anatase and two peaks at 2θ values of 36.14°, 41.34° corresponding to (1 0 1) and (1 1 1) planes of rutile were found.

Sole ZnO XRD exhibited peaks of 2θ values of 31.92° (1 0 0), 34.58° (0 0 2), 36.40° (1 0 1), 47.68° (1 0 2), 56.72° (1 1 0), 62.99° (1 0 3), 66.52° (2 0 0), and 68.08° (1 1 2), 69.20° (2 0 2). ZnO/TiO_2 binary oxides displayed the most intense characteristic peaks at 2θ values of 25.36°-25.44° of (1 0 1) TiO_2 anatase, 27.50°–27.62° of (1 1 0) TiO_2 rutile, and 36.34° −36.40° of (1 0 0) zincite. XRD patterns of the ZT11, ZT13, ZT31 binary oxides expressed ZnO-TiO_2 ratio dependent characteristic variations as could also be visualized by the sharp peaks of zincite in ZT31 and sharp peaks of anatase and rutile phases of TiO_2 in ZT13. On the other hand, ZT11 displayed conforming presence of all peaks of the counterpart oxides.

From characteristic 2θ values of the diffraction peaks, it could be confirmed that respective peaks indicating anatase phase of TiO_2 (JCPDF 21–1272), rutile phase of TiO_2 (JCPDF 21–1276), zincite phase of ZnO (JCPDF 36–1451) were evident. The diffractogram of binary oxides exhibited both anatase and rutile peaks of TiO_2 and zincite peak of ZnO indicating that the ZnO/TiO_2 binary oxides were consisting of only TiO_2 and ZnO. Furthermore, absence of any peaks related to the formation of ternary oxides confirmed that the binary oxides were composed of solely TiO_2 and ZnO [44].

Crystallite size (D, nm) was calculated using the Scherrer equation as:

$$D = K\lambda / (;)$$

Table 1
Physico-chemical properties of the photocatalyst specimens.

Photocatalyst specimen	Anatase crystallite size, nm	Rutile crystallite size, nm	Zincite crystallite size, nm	BET surface area, m^2/g	Pore volume, cm^3/g
TiO_2	20.37	31.48	–	57.55	0.252
ZnO	–	–	33.75	16.62	0.0590
ZT11	20.35	27.94	37.03	29.71	0.0257
ZT13	21.06	27.94	34.58	37.75	0.0315
ZT31	20.63	30.44	35.02	20.37	0.0175

where K = 0.9, λ is the X-ray wavelength being equal to 1.5418 Å for Cu Kα, θ is the Bragg angle and β is the full width at half maximum intensity (FWHM, radians) [45].

The crystallite sizes were calculated from diffraction planes (1 0 1) of anatase TiO_2, (1 1 0) of rutile and (1 0 0) of zincite. The average crystallite sizes of the TiO_2/ZnO binary oxides displayed non remarkable changes with respect to both TiO_2 and ZnO (Table 1). Anatase crystallite sizes were quite similar in all ZnO/TiO_2 samples as well as sole TiO_2 (average = 20.68 nm) whereas rutile crystallite sizes were comparatively smaller (average = 28.77 nm) in comparison to sole TiO_2 (31.48 nm). Zincite crystallite sizes were almost similar in all samples excluding ZT11 expressing slightly higher size (37.03 nm).

Anatase content of the TiO_2 powder was calculated according to the Spurr and Myers equation as:

$$f_A = 1 / (1 + (1.26\ I_R / I_A))$$

where f_A is the weight fraction of anatase while I_R and I_A denote the reflection intensities of rutile (1 1 0) and anatase (1 0 1) respectively [46].

The lattice constants “a” and “c” for TiO_2 and ZnO were determined from two appropriate reflections (h k l) using the following equations respectively:

$$1/d^2 = [(h^2 + k^2) / a^2] + (l^2 / c^2) 1/d^2 = [4/3\,(h^2 + hk + k^2) / a^2] + (l^2 / c^2)$$

where k is the X-ray wavelength equal to 1.5418 Å for for Cu Kα radiation and h is in radians. The value of d (lattice spacing, nm), for an XRD peak can be determined from the 2θ angle by Braggs Law using the following equation:

$$d = \lambda / 2\,s\,in.$$

The peak positions (2θ) of anatase (1 0 1) and (2 0 0) reflections for TiO_2 and zincite (1 0 0) and (0 0 2) reflections for ZnO were used to determine the lattice parameters [47].

Thus calculated lattice parameters of TiO_2 (tetragonal, α = β, γ = 90.0) were a = 3.785 Å and c = 9.423 Å. On the other hand, calculated lattice parameters of ZnO (hexagonal, α = β = 90.00, γ = 120.0) were a = 3.240 Å and c = 5.188 Å. None of these values significantly changed (< 0.1) in binary oxides. The major crystallite phase ratio in sole TiO_2 sample and binary oxides was anatase as expected. The diffraction peak intensities of both anatase and rutile decreased with the increase of ZnO content in binary oxides. Calculated anatase/rutile ratios were around 88.5/11.5 with almost identical crystallite sizes of anatase and rutile. With respect to the effect of calcination temperature applied to the as prepared binary oxides, no significant change in anatase to rutile ratio was expected [48].

SEM image of ZnO indicated the presence of crystallites having various shapes and sizes whereas TiO_2 was consisted of small and spherical particles as aslo reported by various researchers [44,49] (Fig. 2). As a benchmark TiO_2 P-25 is composed of variable-sized rutile/anatase clusters, and the nanoclusters contained typically small rutile crystallites interwoven with anatase crystallites [50].

SEM micrographs of ZnO/TiO_2 binary oxides expressed the

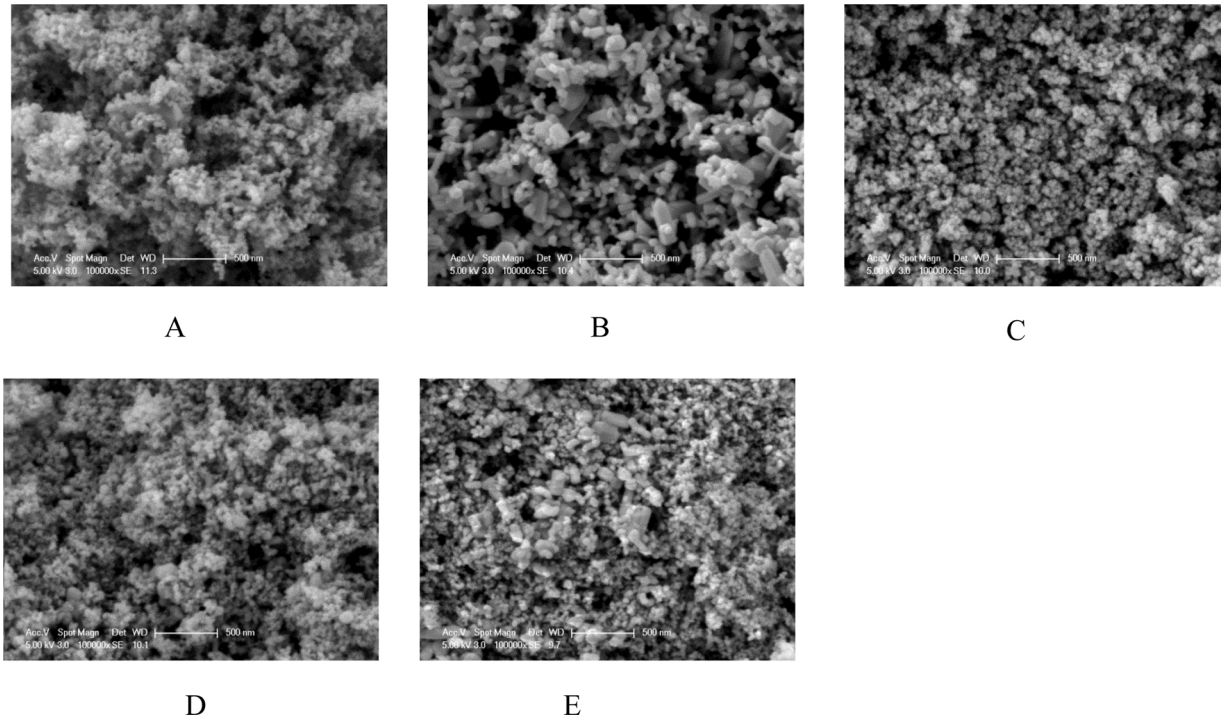

Fig. 2. SEM micrographs A: TiO_2, B: ZnO and ZnO/TiO_2 binary oxides C: ZT11, D: ZT13 and E: ZT31.

morphological characteristics of both counterparts as TiO_2 and ZnO. It was clearly observed that ZT13 contains much more well defined spherical TiO_2 particles than ZT31 due to weight ratio of TiO_2-ZnO in the binary oxide specimen.

XPS spectra was calibrated with respect to C 1s peak. Survey spectra, O 1s spectra, Ti 2p and Zn 2p spectra of the TiO_2, ZnO and ZnO/TiO_2 samples were presented in Fig. 3. XPS survey spectra (Fig. 3A) indicated that all samples contained O, Ti, Zn and C elements. A small amount of carbon peak was emerged due the calcination process during binary oxide preparation. High-resolution spectra of O 1s displayed the peaks at 530.12, 530.14, 530.95, 530.16 and 530.12 eV corresponding to O–Ti bonding of TiO_2 and ZnO bonding of ZnO for TiO_2, ZnO, ZT11, ZT13 and ZT31 respectively (Fig. 3B). FWHM of O 1s peak at 530.95 eV for ZT11 was found to be slightly increased and shifted toward higher binding energy compared with that of the O 1s binding energy in pure TiO_2 due to the overlapping of O–Zn and O–Ti bonding. XPS spectra of Ti 2p contained sharp, symmetric and intense peaks indicating the presence of Ti^{4+} state with two peaks centered at 458.51 and 463.93 eV which were attributed to the Ti $2p_{3/2}$ and $2p_{1/2}$ spin–orbital splitting photoelectrons in Ti^{4+} (Fig. 3C). Ti 2p peaks appeared at 548.83 eV and 463.99 eV were ascribed to Ti $2p_{3/2}$ and Ti $2p_{1/2}$ (O–Ti bond) respectively in pure TiO_2 spectrum. These two binding energies of Ti 2p were also observed in the XPS spectra of ZnO/TiO_2 binary oxides which confirmed the presence of Ti^{4+} state [51,52].

The peak positions of Zn $2p_{3/2}$ and Zn $2p_{1/2}$ were recorded at 1021.22 eV and 1044.11 eV respectively in pure ZnO (Fig. 4D). These two major characteristic peaks of Zn 2p were detected in the spectra of all ZnO/TiO_2 binary oxides.

Raman spectra of sole TiO_2, sole ZnO and binary oxides were displayed in Fig. 4. TiO_2 spectrum expressed four anatase peaks at 137 cm^{-1} (E_g), 386 cm^{-1} (B_{1g}), 510 cm^{-1} (E_g) and 628 cm^{-1} (E_g) and a small rutile peak at 435 cm^{-1} (E_g) indicating the dominant anatase phase of TiO_2 in consistent with the XRD measurements [53].

In ZnO Raman spectrum, peaks at 325 cm^{-1} (E_2 $^{(high)}$–E_2 $^{(low)}$), 383 cm^{-1} (A_1 (TO)), 432 (E_2 $^{(high)}$), 537 cm^{-1} (TO + TA(M)), 577 cm^{-1} (E_1 (LO)), and 653 cm^{-1} (E_2 (low)–B_1 (high)), 707 cm^{-1} (LA + TO), 1125 cm^{-1} ($2A_1$ (LO), $2E_1$ (LO); 2LO) and A_1 (TO) at 381 cm^{-1} corresponded to the strength of the polar lattice bonds. The high-frequency E_2 mode involved predominantly the displacements of lighter oxygen atoms. The very sharp peak at 432 cm^{-1} corresponded to E_2 mode of ZnO. The peak at 577 cm^{-1} E_1 (LO) reflected the multi-phonon and resonance processes which were related to oxygen deficiency. The peak at 1125 cm^{-1} was suggestive of multi-phonon process occurring in ZnO nanoparticles [54–56].

In ZnO/TiO_2 binary oxides, four peaks were observed at ~137 cm^{-1} (E_g), ~390 cm^{-1} (B_{1g}), ~512 cm^{-1} (E_g), and ~632 cm^{-1} (E_g) which coincided with characteristic Raman modes of anatase. The peak at 432 (E_2 $^{(high)}$) of ZnO was only seen in ZT31 sample. Any other peaks of ZnO was not detected due to the low peak intensity of ZnO compared to TiO_2.

UV–vis diffuse reflectance spectra of the specimens displayed a sharp absorption edge at around 380 nm for both of the sole specimens as TiO_2 and ZnO. A slight shift to the red region was observed for the ZnO/TiO_2 binary oxides being more prominent for ZT11 (Fig. 5). The spectral features enabled the calculation of the band gap energies (E_{bg}, eV) of the photocatalyst specimens by the use of the Kubelka-Munk formula as $F(r) = (1-R)^2 / 2R$, where R was the reflectance read from the spectrum, and Tauc equation by plotting $[F(r).h\nu]^n$ vs $h\nu$, where $h\nu$ is the photon energy and $n = 1/2$. The band-gap energies were deduced from the intersection of the Tauc's linear portion extrapolation with the photon energy axis [57].

Band gap energies and corresponding wavelength cut-offs of the samples were found to be in the interval from 3.15 to 3.26 eV and from 394 to 381 nm respectively. ZT31 expressed the lowest E_{bg} following an increasing order as ZT13 < ZT11 < ZnO < TiO_2. A slight shift to visible region of the effective wavelength could be expected to be operating during irradiation under the specified experimental conditions.

PL emission spectra have been widely used to investigate the efficiency of charge carrier trapping, migration, and transfer in order to understand the fate of electron-hole pairs in semiconductor particles since PL emission results from the recombination of free carriers. PL spectra of all specimens were presented in Fig. 6. PL spectrum of pure ZnO consisted of four main emission bands. These bands were a medium UV emission band at λ ~394 nm (3.15 eV), a strong blue band

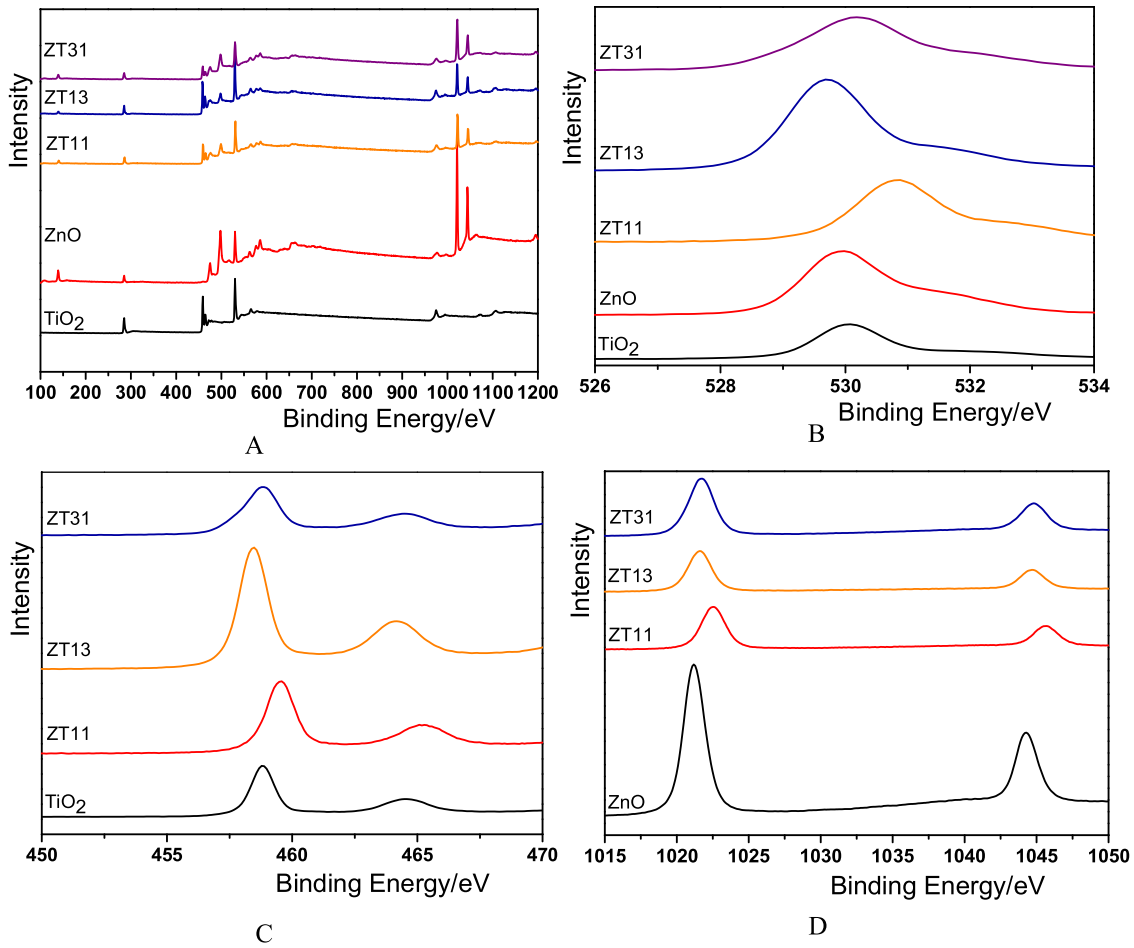

Fig. 3. XPS spectra of TiO_2, ZnO and ZnO/TiO_2 binary oxides A: survey spectra of ZT11, ZT13 and ZT31, B: O 1s, C: Ti 2p, D: Zn 2p.

at ~420 nm (2.96 eV), a blue-green band at ~485 nm (2.56 eV) and weak a green band at ~ 532 nm (2.33 eV) [58]. PL spectrum of pure TiO_2 expressed emission peaks at ~408 nm (3.04 eV), 422 nm (2.94 eV), ~485 nm (2.56 eV) and weak a green band at ~ 532 nm (2.33 eV) showing indirect band gap characteristics [59]. PL spectra of ZnO/TiO_2 binary oxides indicated the presence of peaks at ~394 nm (3.15 eV), ~392 nm (3.17 eV) and ~398 nm (3.12 eV), respectively. The reason was attributed to the different redox energy levels of conduction and valance bands for ZnO and TiO_2 which led to the interfacial charge transfer to inhibit the recombination of electron-hole pairs [60,61].

All samples followed a similar trend in photoluminescence spectra in the wavelength region of $\lambda > 400$ nm. At emission wavelength of $\lambda \approx 420$ nm, the highest PL intensity was attained for ZnO followed by TiO_2 > ZT13 ≈ ZT31 > ZT11 being not discriminately different each other. However, in the emission wavelength region of 425 − 500 nm, a distinct separation was observed for TiO_2 and ZnO couple in comparison to ZT samples being almost equal each other. The trend was also attained at longer emission wavelengths. On the other hand, a sharp increase in PL intensity was attained for all samples in emission wavelength of around 380 nm coinciding with the effective absorption edge of the photocatalyst samples.

BET surface area of TiO_2 was determined as 57.55 m^2/g that was found to be in accordance with the widely reported as 55 ± 15 m^2/g. BET surface area of ZnO as 16.62 m^2/g was quite low in comparison to TiO_2. ZnO/TiO_2 binary oxides were comparatively lower than sole TiO_2 and higher than ZnO in a decreasing order of ZT13 > ZT11 and ZT31. N_2 adsorption-desorption isotherms of the specimens revealed Type IV isotherm with a hysteresis loop associated with mesoporous materials according to IUPAC classification [43]. Pore volumes as determined by BJH method, were found to be in a decreasing order of TiO_2 > ZnO > ZT13 > ZT11 > ZT31. On the other hand, TiO_2 is regarded as nonporous. Respective pore sizes in diameters were in a very narrow range of 2.972-3.632 nm. With respect to the surface morphological properties of the binary oxide photocatalyst specimens, the exposed surface to humic sub-fractions could well be visualized as similar with exception of sole specimens as TiO_2 and ZnO.

The physico-chemical properties of the photocatalyst specimens were compiled in Table 1.

3.2. Photocatalytic degradation of humic acid and kinetic evaluation

Upon use of each photocatalyst, photocatalytic degradation of humic acid as expressed by UV–vis and DOC parameters followed a decreasing profile with respect to increasing irradiation period (Fig. 7).

Kinetics of photocatalytic degradation of HA could be modelled by pseudo first order kinetic model [62].

First order reaction kinetics is expressed as follows:

$$\text{Rate (R)} = -dC/dt = kC$$

Where the terms represent the following meanings;

R: pseudo first order rate (UV–vis parameters: m^{-1}/min, DOC: mg/Lmin),

C: specified UV–vis parameters (m^{-1}) or DOC content (mg/ L),

C_o and C_t: initial concentration and concentration at time t respectively,

t: irradiation time, min,

k: pseudo first order reaction rate constant, min^{-1}.

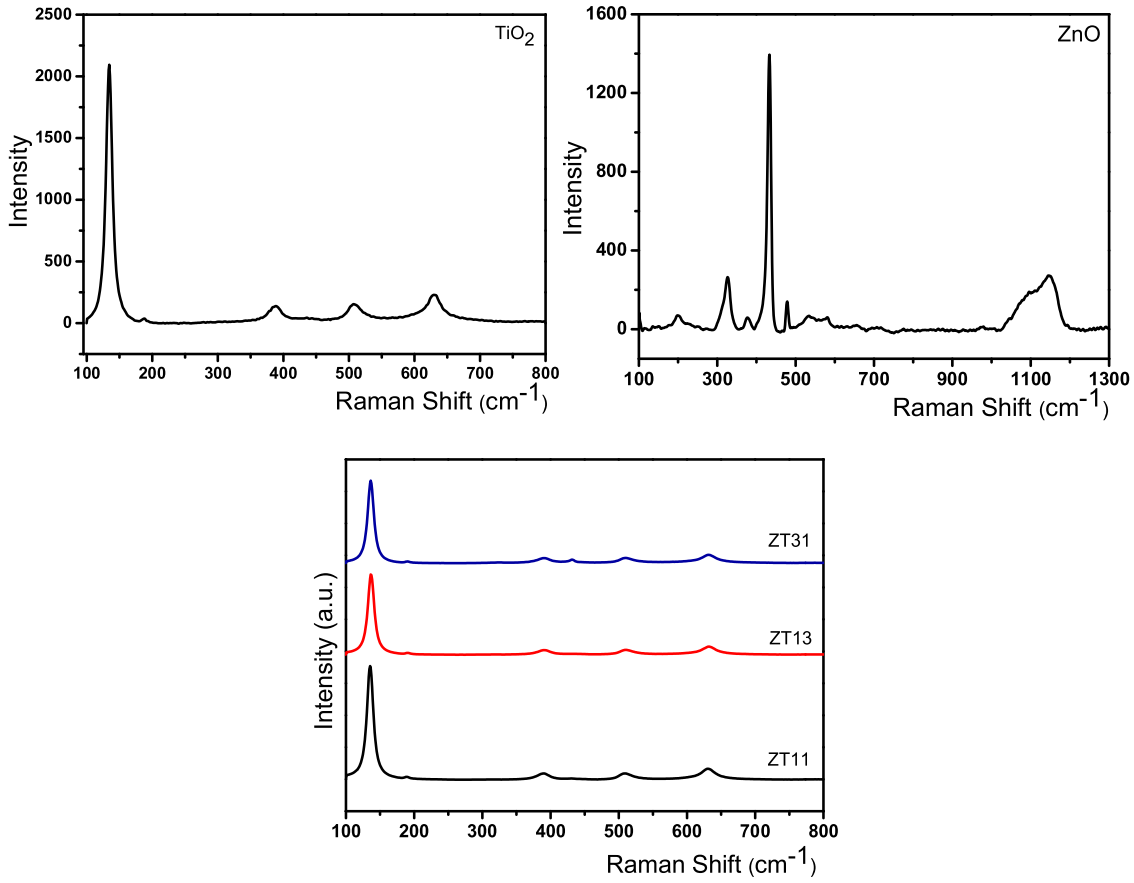

Fig. 4. Raman spectra of TiO_2, ZnO and ZnO/TiO_2 binary oxides ZT11, ZT13 and ZT31.

Half-life ($t_{1/2}$, min) could easily be calculated by the following equation, $t_{1/2} = 0.693/k$.

Besides DOC contents, humic UV–vis parameters could also bring significant information on the oxidative degradation of organic matrix [39,63]. Photocatalytic degradation of 100 kDa HA exhibited the following pseudo first order kinetic parameters (Table 2).

Rate constant of $Color_{436}$ expressed a faster removal upon use of ZnO/TiO_2 binary oxides in comparison to sole TiO_2 and ZnO, whereas removal of UV absorbing centers displayed sample specific inconsistent variations upon use of ZnO/TiO_2 binary oxides in comparison to sole TiO_2 and ZnO. Highest removal rate constant of all UV–vis parameters were calculated for ZT11 contrary to the comparatively lower DOC rate constant. A better visualization could be assessed upon comparison of the half-life values as follows:

Decolorization ($Color_{436}$) half-life values followed a decreasing order of TiO_2 > ZnO > ZT31 > ZT13 > ZT11.

Removal of UV absorbing centers expressed as UV_{254} followed a decreasing order of half-life values as ZT31 > ZnO > ZT13 > TiO_2 > ZT11.

Since PL intensities of photocatalysts are resulting from the recombination of the photoinduced e^-/h^+ pair, they are highly related to the expected photocatalytic activity [43].

These results clearly indicate the selectivity of ZnO and TiO_2 towards photocatalytic degradation of organic matrix that proceeded through various pathways. Since primary surface interactions are expected to play the major role in initiation of photocatalysis, it should be indicated that the highest adsorption of all UV–vis parameters was attained upon use of TiO_2 (~ 15 %) in comparison to all other

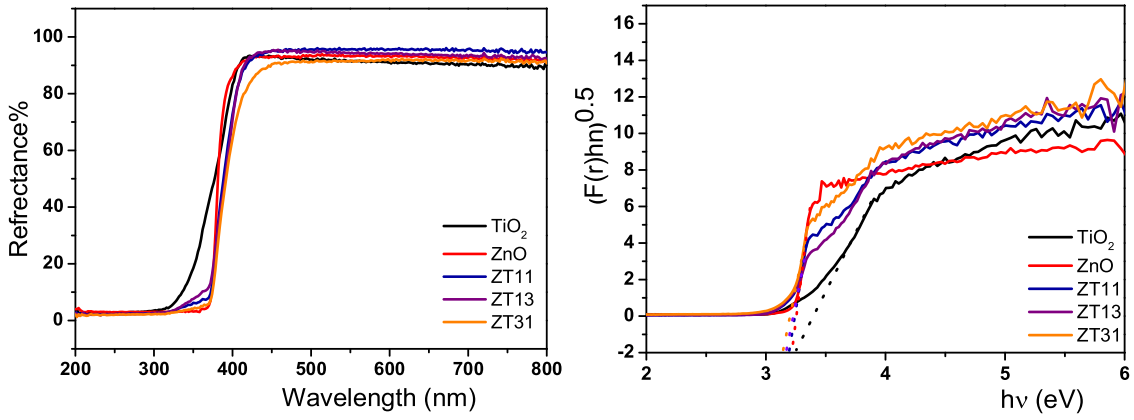

Fig. 5. UV–vis diffuse reflectance spectra A: TiO_2, ZnO and ZnO/TiO_2 binary oxides ZT11, ZT13 and ZT31 and B: respective Tauc plots.

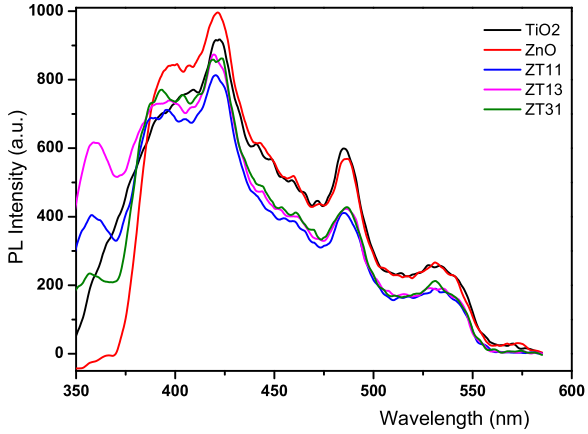

Fig. 6. Photoluminescence spectra of the TiO_2, ZnO and ZnO/TiO_2 binary oxides ZT11, ZT13 and ZT31.

photocatalyst specimens. The initial adsorption extent of all UV–vis parameters were considerably lower upon use of sole ZnO (< 5 %). Incorporation of TiO_2 in ZT specimens reflected as a dose dependent incremental increase in initial surface coverage extent of HA as expressed by UV–vis parameters. On the other hand, with respect to the dose dependent available exposed surface of the specimens, the following sequence of surface coverage extent of organic carbon per unit surface area (DOC g/m^2) was deduced:

DOC_{ads} (g/m^2): ZT11 (0.1723) > ZnO (0.1035) > ZT13 (0.0880) > ZT31 (0.0685) > TiO_2 (0.0578)

The highest surface coverage was achieved for ZT11 and the lowest extent was attained for TiO_2 although the respective extent of UV–vis parameters were significantly higher. The reason could be attributed to the diversity of the humic sub-fractions attracted to the photocatalyst surface. Moreover, it could be deduced from SEM images (Fig. 2) dominance of either TiO_2 or ZnO could strongly affect the morphology of binary oxides which plays a crucial role on the photocatalytic degradation process. Among all binary oxides, ZT11 displayed more homogeneous morphology that could be attributed to the higher performance.

Humic matter is recognized as a dynamic system of aggregational and conformational equilibria among monomers, oligomers and polymers. Due to molecular size dependent physico-chemical heterogeneity of humic matter, reconformation and rearrangement of the sorbed adlayers of humic fractions hold prime importance with respect to effective light absorption capacity of the photocatalysts.

Stability of photocatalyst specimens were elucidated through particle/aggregate size analyses carried both in the absence and presence of HA under dark conditions prior to initiation of photocatalysis. SEM images reflected an aggregation profile of TiO_2 particles in comparison to ZnO and other powder specimens (Fig. 2) [64]. Dispersed particle size distribution profiles of the sole oxide specimens were compared to those measured in the presence of HA (Fig. 8). All samples were prepared in a similar way to sample preparation step prior to initiation of irradiation.

In the absence of HA, with respect to the range of variations in dispersed particle size distribution profiles, the following sequence was attained: ZnO > TiO_2 > ZT11 > ZT13 > ZT31. It could be inferred that the binary oxides displayed quite similar behavior in comparison to the mono-systems. All of the samples were present as aggregates in aqueous medium and could not be dispersed as primary particles [65]. Particle size range was considerably higher for ZT11, almost similar for TiO_2 and ZnO > ZT31 > ZT13.

In the presence of HA, with respect to the range of variations in dispersed particle size distribution profiles, the following sequence was attained: ZnO > TiO_2 > ZT11 > ZT31 > ZT13. It could be inferred that the binary oxides displayed quite similar behavior in comparison to mono-systems. Particle size range was significantly higher for TiO_2 > ZT11 > ZnO > ZT13 > ZT31.

On the other hand, in the absence of HA, time dependent variation of dispersed aggregate sizes of the specimens expressed stable trends excluding ZnO. A very slight size increase was attained for ZnO during a time span of 3 h. The presence of HA did not alter the stability of all specimens except ZnO due to pH dependent surface charge development condition [66]. However, during photocatalysis upon irradiation, the removal and/or formation of new molecular size fractions expressing diverse surface properties could directly affect the aggregate size that could not be followed during photocatalysis.

Therefore, it could be visualized that the primary step of initial DOC adsorption did not necessarily lead to a higher degradation efficiency. During photocatalysis, a continuous photo-adsorption-desorption process could take place between the surface of the photocatalyst specimens and the organic mixture composed of non-oxidized, partially oxidized and even oxidized refractory humic sub-fractions. Thus, the overall photocatalytic degradation efficiencies could neither be directly related to the morphological parameters nor to the initial surface interactions. Upon photocatalysis, mineralization extent as expressed in terms of DOC removal rates followed the sequence of decreasing order as TiO_2 > ZT13 > ZT31 > ZT11 > ZnO.

3.3. UV–vis and fluorescence spectroscopic evaluation of humic acids

100 kDa molecular size fraction of HA expressed UV–vis parameters (cm^{-1}) as $Color_{436}$: 0.1144, UV_{365}: 0.2413, UV_{280}: 0.6012, UV_{254}: 0.7105 and DOC as 5.80 mg/L. An increasing order of carbon based UV–vis parameters were $CbColor_{436}$ = 1.97; $CbUV_{365}$ = 4.16; $CbUV_{280}$ = 10.37 and $CbUV_{254}$ = 12.25 as expected. Since $CbUV_{254}$ > 4 referred to hydrophobic character, 100 kDa molecular size fraction of HA expressed dominance of aromatic core of organic matrix. FI was 1.11 displaying the dominance of humic fluorophores (FI ≤ 1.4) [67].

Elucidation of the photocatalytic degradation mechanism could be related to the understanding of the reactions of the lower molecular size fractions present within the 100 kDa HA macroanion. 100 kDa HA fraction sample was composed of four lower molecular size fractions designated as fr_1, fr_2, fr_3 and fr_4 and defined as < 100 kDa < fr_1 > 30 kDa; 30 kDa < fr_2 > 10 kDa; 10 kDa < fr_3 > 3 kDa; and fr_4 < 3 kDa. Respective UV–vis parameters expressed the following size dependent variations:

$Color_{436}$: 47.0 % fr_1, 30.3 % fr_2, 16.7 % fr_3 and 6.0 % fr_4
UV_{365}: 41.8 % fr_1, 32.2 % fr_2, 20.5 % fr_3 and 5.5 % fr_4
UV_{280}: 36.9 % fr_1, 31.3 % fr_2, 25.7 % fr_3 and 6.1 % fr_4
UV_{254}: 35.5 % fr_1, 31.5 % fr_2, 26.5 % fr_3 and 6.5 % fr_4

Comparatively similar distribution of UV–vis properties within the specified fractions would indicate a rather similar reactivity towards photocatalyst surface both prior to and during light irradiation. From a general perspective, surface interactions proceeds through electrostatic attractions due to pH dependent charge development on the photocatalyst surface as well as humic functional groups mostly expressed by the presence of color forming moieities [38]. Under natural (almost neutral) pH conditions, humic matter could be visualized as partially deprotonated due to carboxylic acid groups (pK_a ~5) and surface of the photocatalyst specimens would acquire positive charge due to pH_{zpc} conditions. More significantly ZnO could exhibit a rather complex situation related to the pH dependent dissolution property [68,69]. The presence of humic matter altered the surface charge of the "reacting complex" reflected as zeta potential decreases to lower values (−30 mV) through shift of charge neutralization phase to charge inversion. Adsorbed humic sub-fractions expressed more hydrophobicity (UV_{254} and UV_{280}) in comparison to color forming moieties. Also, at neutral (natural) pH conditions HA conformational structure could be

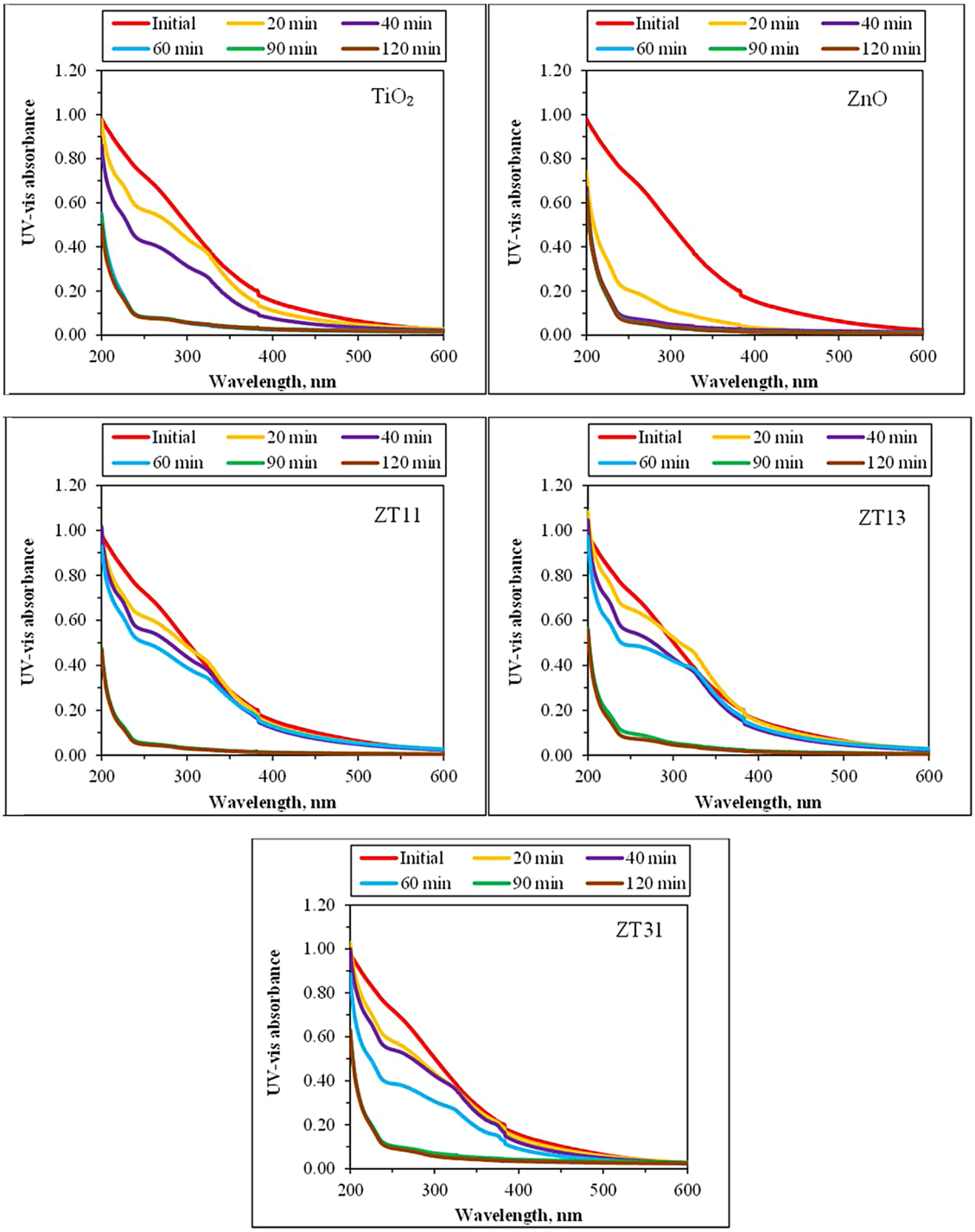

Fig. 7. Irradiation time dependent UV–vis spectral features of humic acid upon photocatalysis.

rather coiled and resembling train-loop-tail type structures. Surface interactions with lower molecular size fractions (< 3 kDa) could well exclude the mesoporous structure of all of the photocatalyst specimens.

Besides kinetics of HA descriptive parameters, carbon based UV–vis parameters hold prime importance revealing information with respect to organic carbon contents (Table 3). $CbUV_{254}$ (also defined as $SUVA_{254}$) displays extent of aromaticity change during treatment [70,71].

Hydrophobicity (> 4) and hyrophilicity (< 3) of humic acids could be assessed by comparison of $CbUV_{254}$. Under prolonged treatment conditions for 120 min at which the remaining DOC contents of all samples were ≤ 2 mgOrgC/L and upon use of sole ZnO and ZnT11, the resultant humic organic matrix displayed hydrophilic character whereas upon use of TiO_2, ZT13 and ZT31, the resultant humic organic matrix retained hydrophobic character. Therefore, it could be indicated that TiO_2 and ZT11 distinctly proceeded through different reaction mechanism in comparison to sole ZnO, ZT13 and ZT31. SFI of HA increased upon photocatalysis indicating the successive removal of fluorophores in accordance with DOC removals irrespective of the type of the photocatalyst specimen.

EEM contour plots display map of fluorophores bringing significant information on the light emitting domains in NOM present in natural waters as well as in wastewaters [72,73]. Photocatalytic degradation of HA has been very well characterized by irradiation time dependent

Table 2
Photocatalytic degradation kinetics of humic acid, Rate constant, $kx10^{-2}$, min and half-life $t_{1/2}$, min ($R^2 > 0.64$).

Photocatalyst specimen	Rate constant, $kx10^{-2}$, min^{-1}				
	$Color_{436}$	UV_{365}	UV_{280}	UV_{254}	DOC
TiO_2	1.426	1.880	2.123	2.164	1.07
ZnO	1.535	1.843	1.862	1.842	0.721
ZT11	2.326	2.674	2.668	2.615	0.735
ZT13	2.076	2.279	2.194	2.127	0.902
ZT31	1.944	1.990	1.752	1.179	0.895
	Half-life, $t_{1/2}$, min				
TiO_2	48.6	36.9	32.6	32.0	64.8
ZnO	45.2	37.6	37.2	37.6	96.1
ZT11	29.5	25.9	26.0	26.5	94.3
ZT13	33.4	30.4	31.6	32.6	76.8
ZT31	35.7	34.8	39.6	58.8	77.4

EEM fluorescence contour plots [52,74].

Excitation-emission matrix fluorophores were assessed by five main reginal distribution profiles; Region I: Aromatic Proteins I (λ_{exc} 220–250 and λ_{emis} 280–332), Region II: Aromatic Proteins II (λ_{exc} 220–250 and λ_{emis} 332–380), Region III: Fulvic-like (λ_{exc} 220–250 and λ_{emis} 380–580), Region IV: Microbial by-products (λ_{exc} 250–470 and λ_{emis} 280–380), and Region V: Humic-like (λ_{exc} 250–470 and λ_{emis} 380–580). Based on EEM contour plots, fluorescence features of HA distinctly expressed the presence of humic-like (region V) and fulvic-like (region III) fluorophores excluding other regional speciation [67]. Following initial adsorption onto TiO_2 and ZnO, the remaining humic organic matrix in solution expressed distinctly different EEM fluorescence features. However upon use of ZT11, ZT13 and ZT31, EEM contour plots of the organic matrix were not significantly different from each other indicating that similar components were predominantly adsorbed onto the surface of the photocatalyst specimens. Moreover, slight distortions in fulvic-like fluorophoric region to aromatic protein-like region should also be expressed (Fig. 9).

For simplicity purposes EEM contour plots recorded upon irradiation period of 60 min were presented. The removal of humic and fulvic like fluorophores could be visualized upon use of TiO_2 and ZnO whereas, these regions were still evident upon use of binary oxides. Moreover, emergence of regions I and II was recorded upon use of TiO_2 being slightly more pronounced in comparison to ZnO. Upon use of the binary oxides, the presence of the resultant fluorophores in almost all regions indicated the transformation of the humic- and fulvic- like fluorophores along with the removal of organic matter by photocatalytic degradation.

Table 3
Carbon based UV–vis and fluorescence properties of HA.

Photocatalyst specimen	Carbon based UV–vis and fluorescence parameters				
	$CbColor_{436}$	$CbUV_{365}$	$CbUV_{280}$	$CbUV_{254}$	SFI
initial	1.97	4.16	10.37	12.25	0.19
TiO_2	1.55	2.27	4.65	5.14	0.33
ZnO	0.50	0.79	2.00	2.43	0.35
ZT11	0.49	0.79	1.97	2.36	0.37
ZT13	0.64	1.18	3.11	3.71	0.38
ZT31	1.53	1.94	3.68	4.55	0.38

4. Conclusions

A novel approach was addressed to the photocatalytic treatment of HA. Besides widely known photocatalysts as TiO_2 and ZnO, binary oxide systems were prepared by a simple solid-solution technique. All photocatalyst specimens were characterized using well described methodologies. 100 kDa molecular size fraction of HA sample was selected excluding higher size fractions and covering medium and lower size fractions (< 100 kDa-3 kDa) expressing quite similar UV–vis spectroscopic properties.

Photocatalytic degradation of HA was followed according to well documented UV–vis and fluorescence techniques supported by advanced fluorescence methods such as EEM fluorescence contour plots.

The performance of thus explained photocatalysts on the degradation of 100 kDa molecular size fraction of HA was expressed by the following order of mineralization extent as: TiO_2 > ZT13 > ZT31 > ZT11 > ZnO.

The results indicated that advantages and disadvantages of two well-known photocatalyst as TiO_2 and ZnO could be balanced through a simple preparation method. The performance of these specimens could be evaluated using a complex organic matrix rather than simple model compounds presented for activity testing.

CRediT authorship contribution statement

Nazli Turkten: Data curation, Investigation, Methodology, Writing - original draft. **Miray Bekbolet:** Conceptualization, Funding acquisition, Project administration, Resources, Supervision, Writing - review & editing.

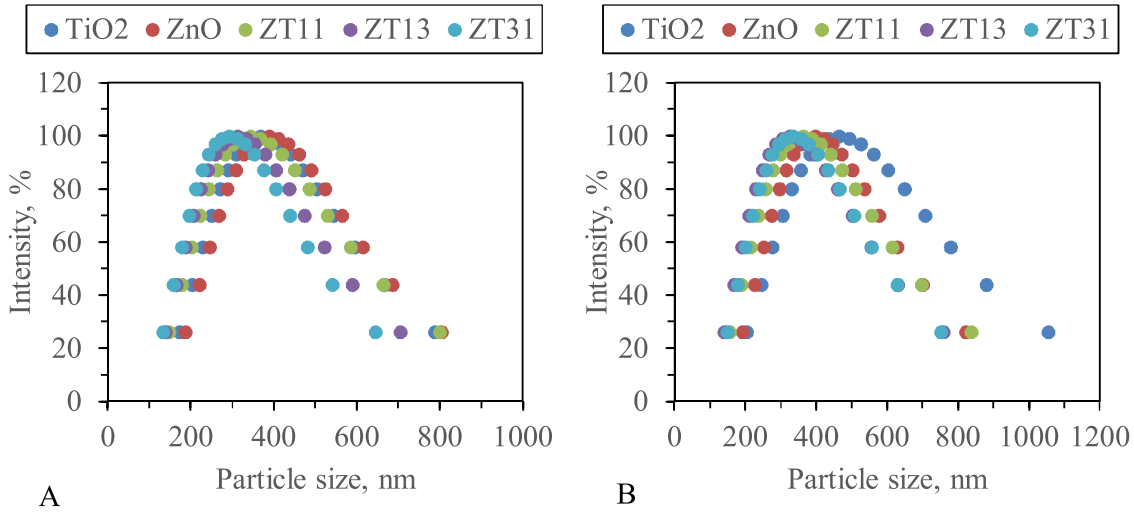

Fig. 8. Dispersed particle size distribution profiles; A: in the absence of HA; B: in the presence of HA.

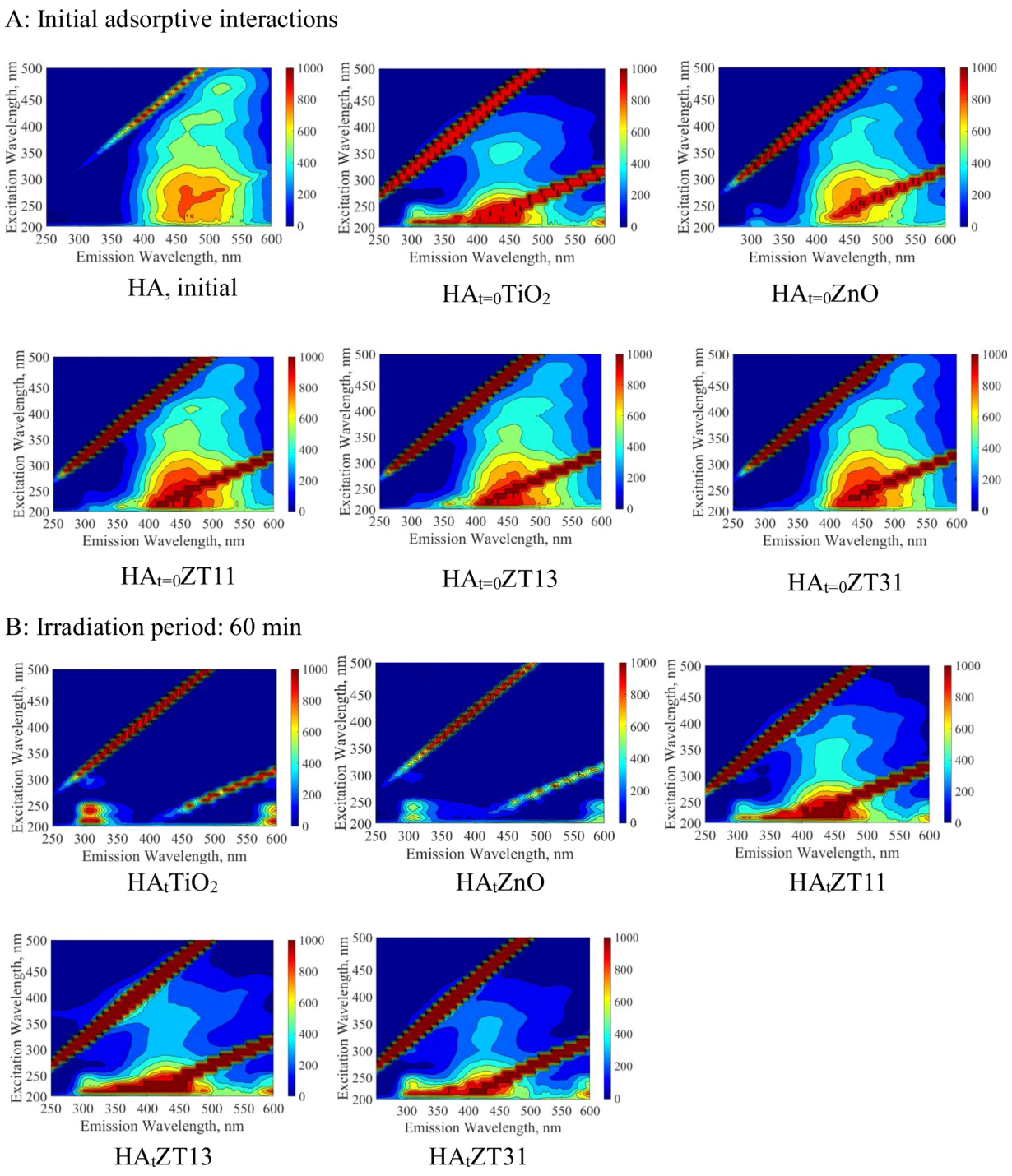

Fig. 9. EEM contour plots of remaining humic organic matrix upon use of TiO_2, ZnO and binary oxides ZT11, ZT13 and ZT31. A: initial adsorption and B: irradiation period of 60 min.

Declaration of Competing Interest

The authors declare that they have no known competing financial interests or personal relationships that could have appeared to influence the work reported in this paper.

Acknowledgement

The authors gratefully acknowledge the support provided by Research Fund of Bogazici University through Project Number 14060.

References

[1] T.A. Egerton, UV-absorption-the primary process in photocatalysis and some practical consequences, Molecules 19 (2014) 18192–18214.
[2] C. Byrne, G. Subramanian, S.C. Pillai, Recent advances in photocatalysis for environmental applications, J. Environ. Chem. Eng. 6 (2018) 3531–3555.
[3] M.A. Henderson, A surface science perspective on TiO_2 photocatalysis, Surf. Sci. Rep. 66 (2011) 185–297.
[4] T. Ohno, K. Sarukawa, K. Tokieda, M. Matsumura, Morphology of a TiO_2 photocatalyst (Degussa, P-25) consisting of anatase and rutile crystalline phases, J. Catal. 203 (2001) 82–86.
[5] H. Zangeneh, A.A.L. Zinatizadeh, M. Habibi, M. Akia, M. Hasnain Isa, Photocatalytic oxidation of organic dyes and pollutants in wastewater using different modified titanium dioxides: a comparative review, J. Ind. Eng. Chem. 26

(2015) 1–36.
[6] A. Di Mauro, M.E. Fragalà, V. Privitera, G. Impellizzeri, ZnO for application in photocatalysis: from thin films to nanostructures, Mater. Sci. Semicond. Process. 69 (2017) 44–51.
[7] K.M. Lee, C.W. Lai, K.S. Ngai, J.C. Juan, Recent developments of zinc oxide based photocatalyst in water treatment technology: a review, Water Res. 88 (2016) 428–448.
[8] K. Qi, B. Cheng, J. Yu, W. Ho, Review on the improvement of the photocatalytic and antibacterial activities of ZnO, J. Alloys Compd. 727 (2017) 792–820.
[9] C.B. Ong, L.Y. Ng, A.W. Mohammad, A review of ZnO nanoparticles as solar photocatalysts: synthesis, mechanisms and applications, Renew. Sustain. Energy Rev. 81 (2018) 536–551.
[10] S. Rehman, R. Ullah, A.M. Butt, N.D. Gohar, Strategies of making TiO_2 and ZnO visible light active, J. Hazard. Mater. 170 (2009) 560–569.
[11] L. Xiang, X. Zhao, Wet-chemical preparation of TiO_2-based composites with different morphologies and photocatalytic properties, Nanomaterials 7 (2017) 310, https://doi.org/10.3390/nano7100310.
[12] M.A. Habib, M.T. Shahadat, N.M. Bahadur, I.M.I. Ismail, A.J. Mahmood, Synthesis and characterization of ZnO/TiO_2 composites and their application as photocatalysts, International Nano Letters 3 (2013) 5.
[13] W.L. Kostedt IV, A.A. Ismail, D.W. Mazyck, Impact of heat treatment and composition of ZnO/TiO_2 nanoparticles for photocatalytic oxidation of an azo dye, Industrial Engineering and Chemistry Research 47 (2008) 1483–1487.
[14] M. Jlassi, H. Chorfi, M. Saadoun, B. Bessaïs, ZnO ratio-induced photocatalytic behavior of TiO_2-ZnO nanocomposite, Superlattices Microstruct. 62 (2013) 192–199.
[15] A. Kubiak, K. Siwińska-Ciesielczyk, Z. Bielan, A. Zielińska-Jurek, T. Jesionowski, Synthesis of highly crystalline photocatalysts based on TiO_2 and ZnO for the degradation of organic impurities under visible-light irradiation, Adsorption (2019), https://doi.org/10.1007/s10450-019-00011-x.
[16] K. Siwińska-Stefańska, A. Kubiak, A. Piasecki, A. Dobrowolska, K. Czaczyk, M. Motylenko, D. Rafaja, H. Ehrlich, T. Jesionowski, Hydrothermal synthesis of multifunctional TiO_2-ZnO oxide systems with desired antibacterial and photocatalytic properties, Appl. Surf. Sci. 463 (2019) 791–801.
[17] P. Cheng, Y. Wang, L. Xu, P. Sun, Z. Su, F. Jin, F. Liu, Y. Sun, G. Lub, High specific surface area urchin-like hierarchical ZnO/TiO_2 architectures: hydrothermal synthesis and photocatalytic properties, Mater. Lett. 175 (2016) 52–55.
[18] A. El Mragui, I. Daou, O. Zegaoui, Influence of the preparation method and ZnO/(ZnO + TiO_2) weight ratio on the physicochemical and photocatalytic properties of ZnO/TiO_2 nanomaterials, Catal. Today 321-322 (2019) 41–51.
[19] S. Liao, H. Donggen, D. Yu, Y. Su, G. Yuan, Preparation and characterization of ZnO/TiO_2, SO_4^{2-}/ZnO/TiO_2 photocatalyst and their photocatalysis, J. Photochem. Photobiol., A 168 (2004) 7–13.
[20] J.T. Tian, J.F. Wang, J.H. Dai, X. Wang, Y.S. Yn, Photocatalyst of TiO_2/ZnO nano composite film: preparation, characterization, and photodegradation activity of methyl orange, Surface & Coatings Technology 204 (2009) 205–214.
[21] Y. Wang, S. Zhu, X. Chen, Y. Tang, Y. Jiang, Z. Peng, H. Wang, One-step template-free fabrication of mesoporous ZnO/TiO_2 hollow microspheres with enhanced photocatalytic activity, Appl. Surf. Sci. 307 (2014) 263–271.
[22] X. Xu, J. Wang, J. Tian, X. Wang, J. Dai, X. Liu, Hydrothermal and post-heat treatments of TiO_2/ZnO composite powder and its photodegradation behavior on methyl orange, Ceram. Int. 37 (2011) 2201–2206.
[23] M. Zhang, T. An, X. Liu, X. Hu, G. Sheng, J. Fu, Preparation of a high-activity ZnO/TiO_2 photocatalyst via homogeneous hydrolysis method with low temperature crystallization, Mater. Lett. 64 (2010) 1883–1886.
[24] X. Zheng, D. Li, X. Li, J. Chen, C. Cao, J. Fang, J. Wang, Y. He, Y. Zheng, Construction of ZnO/TiO_2 photonic crystal heterostructures for enhanced photocatalytic properties, Appl. Catal., B 168-169 (2015) 408–415.
[25] C. Cheng, A. Amini, C. Zhu, Z. Xu, H. Song, N. Wa, Enhanced photocatalytic performance of TiO_2-ZnO hybrid nanostructures, Sci. Rep. 4 (2014) 4181, https://doi.org/10.1038/srep04181.
[26] S. Moradi, P. Aberoomand-Azar, S. Raeis-Farshid, S. Abedini-Khorrami, M.H. Givianrad, The effect of different molar ratios of ZnO on characterization and photocatalytic activity of TiO_2/ZnO nanocomposite, Journal of Saudi Chemical Society 20 (2016) 373–378.
[27] G.K. Upadhyay, J.K. Rajput, T.K. Pathak, V. Kumar, L.P. Purohit, Synthesis of ZnO:TiO_2 nanocomposites for photocatalyst application in visible light, Vacuum 160 (2019) 154–163.
[28] Y. Jiang, Y. Sun, H. Liu, F. Zhu, H. Hengbo Yin, Solar photocatalytic decolorization of C.I. Basic Blue 41 in an aqueous suspension of TiO_2-ZnO, Dyes Pigm. 78 (2008) 77–83.
[29] K. Siwińska-Stefańska, A. Kubiak, A. Piasecki, J. Goscianska, G. Nowaczyk, S. Jurga, T. Jesionowski, TiO_2-ZnO binary oxide systems: comprehensive characterization and tests of photocatalytic activity, Materials 11 (2018) 841.
[30] E.S. Araújo, B.P. da Costa, R.A.P. Oliveira, J. Libardi, P.M. Faia, H.P. de Oliveira, TiO_2/ZnO hierarchical heteronanostructures: synthesis, characterization and application as photocatalysts, J. Environ. Chem. Eng. 4 (2016) 2820–2829.
[31] G.S. Pozan, A. Kambur, Significant enhancement of photocatalytic activity over bifunctional ZnO-TiO_2 catalysts for 4-chlorophenol degradation, Chemosphere 105 (2014) 152–159.
[32] D. Ramírez-Ortega, A.M. Meléndez, P. Acevedo-Peña, I. González, R. Arroyo, Semiconducting properties of ZnO/TiO_2 composites by electrochemical measurements and their relationship with photocatalytic activity, Electrochim. Acta 140 (2014) 541–549.
[33] H. Suo, C. Peng, F. Jing, S. Yu, S. Sheng Cui, X. Shen, Facile preparation of TiO_2/ZnO composite aerogel with excellent antibacterial activities, Mater. Lett. 234 (2019) 253–256.
[34] D. Sethi, R. Sakthivel, ZnO/TiO_2 composites for photocatalytic inactivation of *Escherichia coli*, Journal of Photochemistry and Photobiology, B: Biology 168 (2017) 117–123.
[35] C. Quintiliani, C. Di Cristo, A. Leopardi, Vulnerability assessment to trihalomethane exposure in water distribution systems, Water 10 (2018) 912, https://doi.org/10.3390/w10070912.
[36] N.C. Birben, M.C. Paganini, P. Calza, M. Bekbolet, Photocatalytic degradation of humic acid using a novel photocatalyst: Ce-doped ZnO, Photochemical and Photobiological Sciences 16 (2017) 24–30.
[37] N. Turkten, I. Natali Sora, A. Tomruk, M. Bekbolet, Photocatalytic degradation of humic acids using $LaFeO_3$, Catalysts 8 (12) (2018) 630, https://doi.org/10.3390/catal8120630.
[38] C.S. Uyguner, M. Bekbolet, A review on the photocatalytic degradation of humic substances, in: A. Nikolau, H. Selcuk, L. Rizzo (Eds.), Control of Disinfection by-Products in Drinking Water Systems, NOVA Science Publishers Inc, 2007.
[39] C.S. Uyguner-Demirel, M. Bekbolet, Significance of analytical parameters for the understanding of natural organic matter in relation to photocatalytic oxidation, Chemosphere 84 (2011) 1009–1031.
[40] C.S. Uyguner-Demirel, N.C. Birben, M. Bekbolet, Elucidation of background organic matter matrix effect on photocatalytic treatment of contaminants using TiO_2: a review, Catal. Today 284 (2017) 202–214.
[41] C.S. Uyguner-Demirel, N.C. Birben, M. Bekbolet, A comparative review on the use of second generation TiO_2 photocatalysts: microorganism inactivation, Chemosphere 211 (2018) 420–448.
[42] A. Kerc, M. Bekbolet, A.M. Saatci, Effects of oxidative treatment techniques on molecular size distribution of humic acids, Water Science & Technology 49 (2004) 7–12.
[43] S. Yurdakal, C. Garlisi, L. Özcan, M. Bellardita, G. Palmisano, Photo)catalyst characerization techniques: adsorption isotherms and BET, SEM, FTIR, UV-vis, photoluminescence and electrochemical characterizations, in: G. Marcì, L. Palmisano (Eds.), Heteregeneous Photocatalysis, Relationships With Heterogeneous Catalysis and Perspectives, Elsevier, 2019.
[44] J. Fenoll, I. Garrido, P. Hellín, P. Flores, N. Vela, S. Navarro, Photocatalytic oxidation of pirimicarb in aqueous slurries containing binary and ternary oxides of zinc and titanium, J. Photochem. Photobiol., A 298 (2014) 24–32.
[45] P. Scherrer, Estimation of the size and internal structure of colloidal particles by means of röntgen, Nachrichten von der Gesellschaft der Wissenschaften zu Göttingen 2 (1918) 96–100.
[46] R.A. Spurr, H. Myers, Quantitatively analysis of anatase–rutile mixture with an X-ray diffractometer, Anal. Chem. 29 (1957) 760–765.
[47] B.D. Cullity, Elements of X-ray Diffraction, Addison-Wesley Publishing Company, Inc, London, 1978.
[48] G. Wang, L. Xu, J. Zhang, T. Tingting Yin, D. Han, Enhanced photocatalytic activity of TiO_2 powders (P25) via calcination treatment, Int. J. Photoenergy 2012 (2012) 9, https://doi.org/10.1155/2012/265760 Article ID 265760.
[49] F.A.L. Sánchez, A.S. Takimi, F.S. Rodembusch, C.P. Bergmann, Photocatalytic activity of nanoneedles, nanospheres, and polyhedral shaped ZnO powders in organic dye degradation processes, J. Alloys Compd. 572 (2013) 68–73.
[50] D. Lan, H. Wu, F. Puleo, L.F. Liotta, Bulk and surface characterization techniques of TiO_2 and TiO_2-doped oxides, in: G. Marcì, L. Palmisano (Eds.), Heteregeneous Photocatalysis, Relationships with Heterogeneous Catalysis and Perspectives, L. Elsevier, 2019.
[51] L. Li, X. Zhang, W. Zhang, L. Wang, X. Chen, Y. Gao, Microwave-assisted synthesis of nanocomposite Ag/ZnO-TiO_2 and photocatalytic degradation rhodamine B with different modes, Colloids Surf. A: Physicochem. Eng. Aspects 457 (2014) 134–141.
[52] N. Turkten, Z. Cinar, A. Tomruk, M. Bekbolet, Copper-doped TiO_2 photocatalysts: application to drinking water by humic matter degradation, Environ. Sci. Pollut. Res. (2019) 1–11.
[53] C. Byrne, R. Fagan, S. Hinder, D.E. McCormack, S.C. Pillai, New approach of modifying the anatase to rutile transition temperature in TiO_2 photocatalysts, RSC Adv. 6 (97) (2016) 95232–95238.
[54] T.B. Ivetić, M.R. Dimitrievska, N.L. Finčur, Lj R. Đačanin, I.O. Gúth, B.F. Abramović, S.R. Lukić-Petrović, Effect of annealing temperature on structural and optical properties of Mg-doped ZnO nanoparticles and their photocatalytic efficiency in alprazolam degradation, Ceram. Int. 40 (2014) 1545–1552.
[55] A. Sahai, N. Goswami, Structural and vibrational properties of ZnO nanoparticles synthesized by the chemical precipitation method, Physica E: Low-dimensional Systems Nanostructures 58 (2014) 130–137.
[56] K.J. Chen, T.H. Fang, F.Y. Hung, L.W. Ji, S.J. Chang, S.J. Young, Y.J. Hsiao, The crystallization and physical properties of Al-doped ZnO nanoparticles, Appl. Surf. Sci. 254 (2008) 5791–5795.
[57] P. Kubelka, F. Munk, Ein beitrag zur optik der farbanstriche zeitschrift fur technische physic 12 (1931), pp. 593–620.
[58] S. Labuayai, V. Promarak, S. Maensiri, Synthesis and optical properties of nanocrystalline ZnO powders prepared by a direct thermal decomposition route, Appl. Phys. A 94 (2009) 755–761, https://doi.org/10.1007/s00339-008-4984-2.
[59] D.H. Kim, H.S. Hong, S.J. Kim, J.S. Song, K.S. Lee, Photocatalytic behaviors and structural characterization of nanocrystalline Fe-doped TiO_2 synthesized by mechanical alloying, J. Alloys Compd. 375 (2004) 259–264.
[60] Y. Ku, Y.-H. Huang, Y.-C. Chou, Preparation and characterization of ZnO/TiO_2 for the photocatalytic reduction of Cr (VI) in aqueous solution, J. Mol. Catal. A: Chem. 342-343 (2011) (2011) 18–22.
[61] H. Wang, Z. Wu, Y. Liu, Z. Sheng, The characterization of ZnO-anatase–rutile three-component semiconductor and enhanced photocatalytic activity of nitrogen oxides, J. Mol. Catal. A: Chem. 287 (2008) 176–181.
[62] C.S. Uyguner, M. Bekbolet, Evaluation of humic acid photocatalytic degradation by

UV-vis and fluorescence spectroscopy, Catal. Today 101 (2005) 267–274.
[63] T. Tuhkanen, A. Ignatev, humic and fulvic compounds, update of M. Filella, J. Buffle, and N. Parthasarathy, humic and fulvic compounds, in: P. Worsfold, A. Townshend, C. Poole (Eds.), Encyclopedia of Analytical Science, second edition), Elsevier, Oxford, 2018, pp. 288–298 2005.
[64] D. Jassby, J.F. Budarz, M. Wiesner, Impact of aggregate size and structure on the photocatalytic properties of TiO_2 and ZnO nanoparticles, Environ. Sci. Technol. 46 (2012) 6934–6941.
[65] Y. Zhang, Y. Chen, P. Westerhoff, K. Hristovski, J.C. Crittenden, Stability of commercial metal oxide nanoparticles in water, Water Res. 42 (2008) 2204–2212.
[66] R. Khan, M.A. Inam, Z.S. Zam, D.R. Park, I.T. Yeom, Assessment of key environmental factors influencing the sedimentation and aggregation behavior of zinc oxide nanoparticles in aquatic environment, Water 2018 (10) (2018) 660, https://doi.org/10.3390/w10050660.
[67] S. Sen Kavurmaci, M. Bekbolet, Tracing TiO_2 photocatalytic degradation of humic acid in the presence of clay particles by excitation-emission matrix (EEM) fluorescence spectra, J. Photochem. Photobiol., A 282 (2014) 53–61.
[68] M. Kosmulski, Isoelectric points and points of zero charge of metal (hydr)oxides: 50 years after Parks' review, Adv. Colloid Interface Sci. 238 (2016) 1–61.
[69] F.M. Omar, H.A. Aziz, S. Stoll, Aggregation and disaggregation of ZnO nanoparticles: influence of pH and adsorption of Suwannee River humic acid, Sci. Total Environ. 468-469 (2014) 195–201.
[70] F.H. Frimmel, G. Abbt-Braun, Dissolved organic matter (DOM) in natural environments, in: N. Senesi, B. Xing, P.M. Huang (Eds.), Biophysico-Chemical Processes Involving Natural Nonliving Organic Matter in Environmental Systems, John Wiley and Sons, 2009.
[71] M. Bekbolet, S. Sen-Kavurmaci, The effect of photocatalytic oxidation on molecular size distribution profiles of humic acid, Photochemical and Photobiological Sciences 14 (2015) 576–582.
[72] E.M. Carstea, J. Bridgeman, A. Baker, D.M. Reynolds, Fluorescence spectroscopy for wastewater monitoring: a review, Water Res. 95 (2016) 205–219.
[73] O. Zielinski, N. Rüssmeier, O.D. Ferdinand, M.L. Miranda, J. Wollschläger, Assessing fluorescent organic matter in natural waters: towards in situ excitation–emission matrix spectroscopy, Applied Sciences 8 (2018) 2685, https://doi.org/10.3390/app8122685.
[74] N.C. Birben, C.S. Uyguner-Demirel, S. Sen-Kavurmaci, Y.Y. Gurkan, N. Turkten, Z. Cinar, M. Bekbolet, Comparative evaluation of anion doped photocatalysts on the mineralization and decolorization of natural organic matter, Catal. Today 240 (Part A) (2015) 125–131.

Update

Journal of Photochemistry & Photobiology, A: Chemistry
Volume 417, Issue , 1 August 2021, Page

DOI: https://doi.org/10.1016/j.jphotochem.2021.113281

Journal of Photochemistry & Photobiology, A: Chemistry 417 (2021) 113281

Contents lists available at ScienceDirect

Journal of Photochemistry & Photobiology, A: Chemistry

journal homepage: www.elsevier.com/locate/jphotochem

Erratum to "Photocatalytic performance of titanium dioxide and zinc oxide binary system on degradation of humic matter" [J. Photochem. Photobiol., A 401 (2020) 112748]

Nazli Turkten [a,*], Miray Bekbolet [b]

[a] Department of Chemistry, Faculty of Arts and Sciences, Kirsehir Ahi Evran University, Kirsehir, 40100, Turkey
[b] Institute of Environmental Sciences, Bogazici University, Bebek, Istanbul, 34342, Turkey

The publisher regrets that the below mistakes were found in the published paper.

1) In Page 3, "Scherrer equation", the denominator part of the equation was missing.

The corrected equation is:
Crystallite size (D, nm) was calculated using the Scherrer equation as:

$$D = K \lambda / (\beta \cos\theta)$$

2) In Page 3, two equations stated after this sentence "The lattice constants "a" and "c" for TiO_2 and ZnO were determined from two appropriate reflections (h k l) using the following equations respectively" was written in a combined style. However, the equations should be written separately.

$$1/d^2 = [(h^2 + k^2) / a^2] + (l^2 / c^2)$$

$$1/d^2 = [4/3\ (h^2 + hk + k^2) / a^2] + (l^2 / c^2)$$

3) In Page 3, "Braggs Law using the following equation" was written without a denominator.

The corrected equation was:

$$d = \lambda / 2\sin\theta$$

The publisher would like to apologise for any inconvenience caused.

DOI of original article: https://doi.org/10.1016/j.jphotochem.2020.112748.
* Corresponding author.
E-mail address: nazli.turkten@ahievran.edu.tr (N. Turkten).

https://doi.org/10.1016/j.jphotochem.2021.113281

Available online 24 May 2021
1010-6030/© 2021 Published by Elsevier B.V.